

AE803

Interpretation of the Dynamic Response of a Masonry Arch Rail Viaduct using Finite Element Modelling

Sam Cocking¹, Sinan Acikgoz² and Matthew DeJong³

¹PhD Student, Department of Engineering, University of Cambridge, Trumpington Street, CB2

1PZ, sc740@cam.ac.uk, corresponding author

²Associate Professor, Department of Engineering Science, University of Oxford, Parks Road, OX1

3PJ, sinan.acikgoz@eng.ox.ac.uk

³Assistant Professor, College of Engineering, University of California, Berkeley, 320 McLaughlin

Hall, CA 94720-1700, dejong@berkeley.edu

ABSTRACT

Linear-elastic finite element analysis is sometimes used to assess masonry arch bridges under service loads, despite the limitations of this method. Specifically, linear-elastic analysis can be sensitive to material properties, geometry, and support settlements, while also allowing the development of tensile stresses which may be unrealistic for masonry structures. However, even though linear-elastic methods remain appealing for their simplicity, it is rare to evaluate their output against experimental data. In this paper, detailed strain and displacement monitoring data for a masonry arch viaduct is used to evaluate a series of independently developed linear-elastic simulations of this structure. Although uncertainties in input parameters mean the magnitude of modelling results cannot be presumed accurate, the

simulated response pattern was found to agree reasonably well with monitoring data, in regions of low damage. However, more damaged regions produced a markedly different local response. Comparisons between the simulations revealed useful conclusions regarding common modelling assumptions, namely the importance of modelling backing material, spandrels, and foundation stiffness, to capture their influence on the arch response.

Keywords: Masonry Arch; Finite Element Modelling; Structural Health Monitoring

INTRODUCTION

Context

Masonry arch bridges form a major part of the transport networks in Europe, for both road and rail. There are over 200,000 of these structures in Europe (Brencich & Morbiducci, 2007). In the UK alone, there are approximately 70,000 (Armstrong, Sibbald & Forde, 1995). It is estimated that between 40 and 50% of bridge spans on the UK road and rail networks are masonry arches (Augusthus-Nelson *et al.*, 2016).

Many of these structures are now approaching 150 years old and maintenance is an increasingly pressing concern. Speed and weight restrictions might be imposed on assets which show large movement under their live loads. Meanwhile, transport networks face increasing demands from their users. This places engineers under pressure to justify any restrictions, which in turn creates a strong motivation to better assess the expected live load responses of these structures. This is a difficult task, which is typically approached using computational analysis models.

Current Assessment Approaches

The choice of analysis type should be informed by the fundamental behaviour of masonry structures, and in particular by both the current damage state of the structure under consideration and the magnitude of its loading with respect to the ultimate collapse load. For example, while limit state techniques are well-established and allow for good understanding of the collapse behaviour of masonry structures, they cannot provide information on the response under low-magnitude working loads.

Masonry gravity structures tend to have significant dead loads leading to compressive stresses, before the application of their live loads which may themselves elicit either compressive or tensile stresses. This compressive baseline due to dead loads allows for the safe operation of masonry structures because, even after live loads are applied, resultant stresses should remain compressive. Furthermore, as long as these loads are not too high in magnitude, stress-strain behaviour may be assumed linear elastic.

However, there are several factors which can cause damage and affect the baseline stress, meaning that any estimate of this baseline is highly uncertain. This can happen independently of any applied loading. Firstly, the inherent weakness of historical lime mortars means that minor cracking can easily arise, for example when centring is struck following the construction of an arch. Cracking such as this does not necessarily mean that the arch is in danger and the overall arch behaviour should remain linear-elastic even if some minor cracks are present. In the case of large settlements, large cracks may occur in masonry, which will have an influence

on the 'initial' state of stress in masonry. This will have an impact on the subsequent response of the structure to loading.

Detailed analysis of the precise dynamic response of masonry arch structures with a significant amount of existing damage, such as major cracking, would require the use of complex three-dimensional nonlinear computational models. Such models would seek to capture the realistic behaviour of the masonry and soil materials, along with interaction effects between different structural components, such as the arch barrel, backfill, spandrel walls, piers and foundations, as well as including detailed modelling of damage (Domede, Sellier & Stablon, 2013). Numerous examples of complex 2D and 3D finite element (FE) analyses exist in the literature (Fanning & Boothby, 2001; Gibbons, 2014; Zhang, Macorini & Izzuddin, 2017).

An alternative approach is to use Discrete Element Modelling (DEM). In this, masonry structures are represented as assemblages of rigid blocks, which can overcome their surrounding bonds and move relative to one another. This approach has been shown to reasonably capture the behaviour of dry-stone masonry structures, and has been applied by many researchers (e.g. Lemos, 2007; DeJong & Vibert, 2012; McInerney & DeJong, 2015; Costa *et al.*, 2015; Forgács, Sarhosis & Bagi, 2017). DEM methods are ideally suited for modelling large displacements, separation and re-contact of discrete block structures, and collapse, but present computational challenges when modelling material deformation and damage such as cracking.

For asset management of masonry arch bridges with a complex history of damages and repairs over decades, it is often impractical to employ the complex procedures described above. Instead, typical assessments may only address safety at the ultimate limit state (ULS),

which corresponds to the point of collapse. Ultimate conditions can be investigated through a simplified limit state analysis; software commonly used for this purpose includes ARCHIE-M (Harvey, 2017) and LimitState:RING (Gilbert, 2017). The collapse loads found are related back to working conditions by means of an adequacy factor, but serviceability behaviour is not explicitly considered. However, since the response under working loads will drive the deterioration of these structures, it is warranted to examine serviceability behaviour directly. Indeed, the concerns of asset managers are often serviceability issues, such as large deflections, progressive cracking, or a lack of transverse load transfer.

When an asset engineer is concerned about the performance of a bridge, they may commission monitoring to gauge the current level of response and to track how this changes with time. For example, in the UK, Network Rail sometimes measures vertical deflections at the arch crown, under the action of train loads. In these cases, it would be useful to know typical values for deflections of the arch crown for a given linear elastic bridge as a point of comparison. The influence of previous and emerging damage on the bridge can then be observed by comparing monitoring data to simulations.

Scope of Study

In this study, the severity of the bridge's current condition is investigated by comparing the true, monitored response of the "as-is" bridge against a simulated pre-damage response corresponding to its original linear-elastic behaviour, produced using FE models of the undamaged "as-built" bridge. In particular, FE models have been used to investigate the Marsh

Lane viaduct, located in Leeds, UK. Monitoring data had previously been established which illuminated its structural response under operational loads (Acikgoz *et al.*, 2018a).

This study is concerned with the evaluation of the FE simulations with respect to monitoring data, rather than the interpretation of the monitoring data itself. Specifically, in this paper, linear-elastic FE modelling results are compared to monitoring data in order to evaluate:

1. The extent to which the real behaviour deviates (both in displacement and strain distribution) from an undamaged elastic response. It is hypothesised that these deviations represent nonlinearities which could indicate the extent and location of damage to the viaduct.
2. The relative importance of modelling each component of the arch bridge (such as spandrel walls, backing material between the arch haunches, and relieving arches in the piers). This is evaluated by comparing FE models with different levels of complexity against one another, as well as against monitoring results. From this, conclusions are drawn regarding the importance of common modelling assumptions for masonry arch bridges.

Other researchers have investigated the relative importance of these structural components experimentally for the ULS case, and suggested percentage increases of the ultimate capacity which result from the inclusion of features such as fully-connected spandrel walls and the arch-backfill interaction (Boothby, Domalik & Dalal, 1998; Fanning, Boothby & Roberts, 2001; Brencich, Cassini & Pera, 2016). However, this computational study focuses on SLS conditions.

BACKGROUND – MARSH LANE VIADUCT

Overview of the Viaduct

Previous monitoring work by the Cambridge Centre for Smart Infrastructure and Construction (CSIC) has measured the service response of the Marsh Lane viaduct; this monitoring is reported in a separate paper (Acikgoz *et al.*, 2018a). The viaduct dates from the 1860s and has a total of 93 arch spans. Arches 37 and 38 are the two which are considered in detail in this study, as they show the most damage and so were the focus of the monitoring installation. The location of these arches is shown in Figure 1, which is adapted from a Network Rail map (Network Rail, 2013).

All main components of the superstructure are built using the conventional brickwork and weak lime mortar of the time. The only exceptions are the skewbacks, which consist of stone blockwork, and the internal backing above the piers. The composition of the backing is not known but is believed to be either concrete or rubble masonry. Above this lies the soil backfill and ballast supporting the rails. Drawings of the substructure do not exist; however, taking account of typical construction details for the period, the most likely case is concrete strip foundations underneath each pier.

The viaduct (shown in Figure 2, with key dimensions in Figure 3) shows signs of deterioration from its long working life, which have given rise to visible deflections under live load. Prior to monitoring, Network Rail commissioned repair work to address this damage; this included the fitting of tie bars through the spandrel walls and the filling in of the relieving arches with concrete, in an attempt to arrest development of significant existing cracks in the arch soffits, primarily located near to the arch haunches but in some cases extending towards

the arch crown. This latest intervention seems to have had a positive impact, as the rate of propagation of cracks close to the arch haunches has since declined. This has been noted in recent inspections of the bridge. However, deflections remained visible following these interventions, and so monitoring was conducted in order to understand the key drivers of this behaviour.

Figure 4 indicates the key damage affecting arches 37 and 38, on either side of their shared pier. Pronounced longitudinal cracks spring from just above the pier relieving arches and extend up to the third points of the arch spans. Transverse cracks are also present and consistently occur close to the tops of the arch haunches, at a vertical level corresponding to the height of internal rigid backing. Further longitudinal cracking is found on the soffits along the interfaces between the arch barrels and the spandrel walls, and this is supplemented by horizontal cracking on the spandrel walls themselves. Finally, it is worth noting that hammer tapping on the arch soffit did not indicate appreciable ring separation. The damage at Marsh Lane viaduct is documented in (Acikgoz *et al.*, 2018a) and has been studied in detail through comprehensive laser scanning, which suggests that settlement of the pier between arches 37 and 38 could explain the increased severity of the damage affecting these arch spans (Ye *et al.*, 2018).

Monitoring Data

Details of the monitoring scheme were presented by (Acikgoz *et al.*, 2018a) and will only be summarised briefly here. The installation used Fibre-Bragg Grating (FBG) sensors, embedded in fibre-optic cables, to measure in-plane strains at locations on the arch soffit and piers of the two adjacent spans of arches 37 and 38, while digital image correlation with commercial video cameras was used to capture displacements and rigid body rotations.

FBGs measured strain along two longitudinal lines on each monitored arch barrel; the lines were positioned to lie directly underneath the centrelines of the two railway tracks. Each line recorded data at eight locations, labelled S1 to S8 and distributed symmetrically across the arch intrados, in addition to the pier-to-pier span opening. Separate FBGs measured transverse strains in the arch barrel, as well as pier strains.

The locations of the longitudinal FBG monitoring lines, which are of most relevance to this study, are indicated in Figure 5. This figure shows the monitoring locations on the arch soffits as viewed from ground level. The notation in this study is such that, as the train passes over each barrel, S1 is the first FBG that the leading axle passes above and S8 is the last, irrespective of the direction in which the train is travelling. The approximate locations of the rail tracks are also shown in Figure 5, with dotted lines.

Data Used in this Study

From the monitoring data, two representative datasets were chosen for use in this study. These captured the response of the viaduct under a three-carriage Class 185 train, travelling East in one dataset and West in the other. This allowed investigation of the responses of both halves of the viaduct, where similar response was expected. Class 185 trains are the most common loading experienced by the viaduct; furthermore, their long wheelbase of 16m, which is the distance between the bogie centres of each carriage, is approximately twice the span length of the viaduct arches and therefore caused the most significant span opening response. These dynamic loads, as the trains travelled over the viaduct, were found to result in a pseudo-static response which was repeatable with little variation between trains, suggesting that the variation in live loads due to passengers is unimportant (Acikgoz *et al.*, 2018a). Typical axle

loads for class 185 trains were applied in the models: 32.2 tonnes for the leading bogie of each carriage and 34.4 tonnes for the rear bogie.

Comparisons between monitoring data and finite element simulations were made for the span-to-span opening displacement, crown vertical displacement, crown in-plane strain and the barrel in-plane strains at points S1 to S8. The in-plane strains offered most insight into the overall mode of deformation of the arches, and the variation of this mode between current real behaviour and the “pre-damage” FE models.

An example of the monitored span opening response is shown in Figure 6. Here, responses from all four longitudinal monitoring lines are shown, both for the case where trains are passing directly overhead (Figure 6, top row) as well as the response that is measured when trains pass on the other track (Figure 6, bottom row). The response is considerably larger for the northern monitoring lines L1 and L3, where significant damage has concentrated. In these signals, peaks correspond to span opening, which occurs when axle loads are applied directly above the span; meanwhile troughs correspond to span contraction, which occurs when the train is positioned such that axle loads are only applied to the adjacent spans either side of the arch under consideration. This interaction effect between adjacent spans is visualised later in Figure 8; however, spans that are further away are found to have a negligible impact. Here, $\Delta WP - EP$ is used to denote pier-to-pier span opening and is measured by a single FBG that is clamped between the tops of the two piers. τ is a normalised time. It is determined by identifying the two largest peaks of the response, which correspond to the leading and rear bogies of the train, and then equalising the time between these peaks. This allows the evaluation of multiple datasets, from trains with different speeds, within the same plot.

METHODOLOGY – FINITE ELEMENT MODELLING

Overview

A series of FE models of the viaduct were built using Abaqus FEA software, each including progressively more structural detail for the superstructure of the viaduct. This allowed the relative stiffness contributions of each major structural component to be assessed. These models are shown in Figure 7:

- a) A basic model of the piers and arches
- b) Model 1 with spandrel walls added
- c) Model 2 with rigid backing modelled up to the underside of the soil fill
- d) Model 3 with relieving arches added to the piers

In Model 1, the dead loads of the spandrel walls and backing material have been applied to the arches, but these components are not explicitly modelled. In this way, the arches respond independently to the applied loads, as might be expected for a heavily damaged viaduct that has lost continuity between these components due to significant cracking. The exclusion of spandrel walls and backing from models of damaged arch bridges is a common assumption. However, this causes an overestimation of SLS behaviour.

In Models 2 and 3, these structural components are now explicitly modelled and are assumed to have full connectivity with the arches. Now, the overestimation of response may be avoided, however, the assumption of full connectivity is not realistic for damaged viaducts, which exhibit some degree of separation cracking between these structural components. Based on typical construction details for the time, it is assumed that the backing material above the

piers is either concrete or rubble masonry, and therefore provides significant stiffness compared to the adjacent soil. Therefore, the backing is modelled indirectly by rigidly tying the arch haunches together across the top of their shared pier.

In FE Model 4, relieving arches in the piers are included. These have the effect of reducing the stiffness of the piers, which could potentially lead to larger span-to-span opening displacements.

In reality, there is likely to be partial connectivity between the arches and their adjacent structural components. Thus, the measured, true response of the bridge is compared with the limiting cases of these simplified models to see which, if any, is most representative.

In each of these models, homogeneous continuum shell elements (types S3R and S4R) have been used to represent the masonry. Five integration points were specified across the thickness of each element. Surface strains were extracted from the extreme integration point at locations of interest on the arch intrados. When rigid ties were included, these were achieved using slave-master node relationships.

Each model consisted of five arch spans. The outer two arches existed purely to apply boundary conditions without influencing the results of the central span, which were compared against monitoring data. Live loads were applied pseudo-statically to the central three spans, in order to capture the interaction effects of adjacent spans on the central arch.

Dead loads were modelled in an initial analysis step, before the application of live loads. These live loads, which in reality are travelling point loads applied by the train axles to the tracks, were modelled directly at the arch extrados in the FE models. Following distribution

through the backfill, each axle load becomes spread out into an area load which acts over a region of the masonry arch. This load is then transferred from the backfill into the arch as a pressure, which acts in the normal direction of the arch. By applying the train loads directly as normal pressures, it was possible to avoid modelling the soil backfill material explicitly in the FE simulations. Distribution was calculated separately, assuming a half-angle of distribution of 15° through the ballast and 30° through the fill. These values come from Network Rail guidance (Network Rail, 2006). Any possible distribution through the sleepers was neglected. These calculations were repeated for nine distinct locations, corresponding to salient points of the span-to-span opening response. The nine analysis steps are shown in Figure 8, along with the corresponding locations of axle loads at these times. In particular, it should be noted that there is clear repetition in the span-to-span opening response, which allows these nine analysis steps to describe any Class 185 train with an arbitrary number of carriages. The three distinct components of the response correspond to bogie locations shown in the three rows of the grid in Figure 8. The top row (steps 1 to 3) shows the leading bogie of the train, which produces the peak span opening at the start of the response; by reversing the order of these analysis steps they can also represent the rear bogie of the train, which produces an equally large span opening displacement at the end of the response. The remaining analysis steps correspond to points at which there is interaction between two bogies. The second row (points 4 to 6) represents the case when the leading and rear bogies of an individual carriage are applied to the two spans either side of the arch under consideration, resulting in span closing. In the third row, the rear bogie of one carriage interacts with the leading bogie of the carriage behind it, giving rise to the characteristic double peak described by points 7 to 9.

Assumed Input Parameters

It was not possible to perform in-situ material testing at Marsh Lane viaduct, and so input parameters had to be estimated. This is often the case when a masonry arch bridge is to be modelled, and as a result there can be high uncertainty in the output of any computational simulation. It is important to note that the following assumptions for this study were arrived at by investigating the likely values and comparing them primarily to the $\Delta W P - E P$ signal. Later, the simulation data is compared to other signals, which were not involved in the calibration of the model.

Likely values of masonry Young's modulus and density were taken from the literature (EUCENTRE, 1987; Augenti, Acconcia & Parisi, 2012). Upper values from the most probable ranges were specified, representing the maximum possible stiffness that a simplified linear-elastic model could offer.

The soil springs were calculated using the empirically-fitted Wolf's equations for embedded foundations (Wolf, 1994). These are summarised below in equations (1) to (3). To express these in terms of the soil Young's Modulus, the definition of Shear Modulus G_{soil} is applied as shown in equation (4).

$$K_r = \frac{G_{soil}b^3}{1-\nu_{soil}} \left[3.73 \left(\frac{l}{b} \right)^{2.4} + 0.27 \right] \left[1 + \frac{e}{b} + \frac{1.6}{0.35 + \left(\frac{l}{b} \right)^4} \left(\frac{e}{b} \right)^2 \right] \quad (1)$$

$$K_h = \frac{G_{soil}b}{2-\nu_{soil}} \left[6.8 \left(\frac{l}{b} \right)^{0.65} + 2.4 \right] \left[1 + \left(0.33 + \frac{1.34}{1 + \frac{l}{b}} \right) \left(\frac{e}{b} \right)^{0.8} \right] \quad (2)$$

$$K_v = \frac{G_{soil}b}{2-\nu_{soil}} \left[3.1 \left(\frac{l}{b} \right)^{0.75} + 1.6 \right] \left[1 + \left(0.25 + \frac{0.25b}{l} \right) \left(\frac{e}{b} \right)^{0.8} \right] \quad (3)$$

$$\text{where } G_{soil} = \frac{E_{soil}}{2(1 + \nu_{soil})} \quad (4)$$

In these equations, $2b$ is the foundation's length and $2l$ is its width. Rotation is assumed to occur about the "length" axis. The embedment from ground level to the underside of the foundation is denoted by e . E_{soil} and ν_{soil} are the Young's Modulus and Poisson's ratio for the soil, respectively.

The vertical soil spring from equation (3) was recalibrated based on observations of vertical pier deflection under load; it was found that Wolf's equations under-predicted this stiffness. Unfortunately, there was no information against which to calibrate the other two soil springs, and so the original values from Wolf's equations have been kept in these cases.

For the Marsh Lane viaduct, the assumed geometry below ground level is as shown in Figure 3(b). The foundation dimensions and embedment have been estimated based on guidance from Network Rail. Based on this, the foundations were taken to be 0.5 m deep concrete strips which extended beyond the plan dimensions of the piers by 0.5 m in all directions. The embedment was found by assuming that inverse relieving arches existed immediately below ground level, giving an overall embedment of 2.4 m below ground level.

Table 1 summarises the values of input parameters that were ultimately used. For the soil springs, Table 1 presents individual stiffness values that describe the global response of each embedded pier, as this is the form that is yielded by Wolf's equations. However, in the FE models, these are then distributed over a row of springs, one at each node along the length of the pier.

Boundary Conditions

The model is restrained against longitudinal and vertical translation at the outer two arch barrels, along their furthestmost springing lines. The outer edges of the spandrel walls are also restrained against longitudinal translation, as well as against rotation about the global vertical axis. These conditions represent the restraint provided by the rest of the viaduct superstructure and are illustrated in Figure 9. No site investigations into the foundation and soil conditions exist at the Marsh Lane viaduct, beyond a qualitative assessment of the soil conditions which rated the soil as a sandy clay, which was used to estimate likely values.

The vertical soil springs, of total stiffness K_v , are distributed along the pier bases. The horizontal springs are distributed along a line of nodes at the mid-depth of the embedded region; these have a combined total stiffness of K_h . However, on the outer piers these springs are replaced by ground-level pins, preventing any horizontal movement. These pins, although unphysical, are required as a boundary condition to achieve physically acceptable behaviour of the outer piers; since the dead load of the superstructure is not modelled beyond these piers, they tend to deflect outwards unrealistically when the pins are not applied. Furthermore, all the pier bases are restrained against rotation about the global transverse axis by rotational springs. For each pier these springs have total stiffness K_r , but once again these have been modelled by distributing this stiffness over the length of the pier.

Figure 9 illustrates the above boundary conditions and soil springs. Additionally, and not shown in Figure 9, the pier bases are restrained against rotation about the global vertical and longitudinal axes. Furthermore, the centre points of each pier base are pinned against

translation in the transverse direction. This transverse boundary condition was kept to a single point as it was not desirable to over-constrain the model.

The impact of these boundary conditions was assessed by comparing pier-to-pier deflections over the central span of two model versions, one with five spans and another with seven. The results are shown later in Figure 13(b), which compares the span-to-span opening response of two versions of Model 4. The difference in results is negligible. This suggests that, when five spans are modelled, the boundary conditions are already far enough removed from the central span that they do not influence the results. Similar checks yielded the same results for the other three FE models.

RESULTS

1) Comparison of Monitoring Data and Modelling Results

Throughout model development, pier-to-pier span opening was used to compare the results of FE models against the monitored behaviour of the real viaduct. Figure 10 shows a typical pier-to-pier response, as measured by FBG sensors, and compares this against results for FE Models 1 to 4.

Having developed the models against the benchmark of the pier-to-pier response, agreement between the linear-elastic FE simulation and the monitoring data was investigated for other parameters. Figure 11 compares vertical displacements at the arch crown from FE Model 4 against values that were observed using digital image correlation (Acikgoz *et al.*, 2018b). Similarly, in-plane crown strain is also shown in Figure 11; the measured values here were obtained from FBG data. For completeness, the earlier comparison for pier-to-pier span

opening is also included. In this figure, the modelling results are compared against monitoring data for all longitudinal lines, denoted L1 to L4 as in Figure 5.

Figure 12 then compares the in-plane barrel strains at FBG monitoring locations S1 to S8. Strains from the FE analysis have been averaged over the same 1m gauge lengths that the FBGs used and measured in the same longitudinal planes.

2) Contributions of Structural Components to Overall Behaviour

Based on the information contained in Figure 10, which compared the pier-to-pier response for the four FE models against FBG monitoring data, it is possible to ascertain the relative resistance that is provided by each of the models against pier-to-pier opening. The final FE model is chosen as a benchmark of 100% resistance because it contains all key structural components; other models are compared against this. Since the models will scale equally if different input parameters are used, this comparison between models is independent of the parameters that have been used in this case. In effect, this gives the relative contributions of the various structural components to overall serviceability behaviour. These results are given in Table 2.

The final FE model can also be compared against the measured FBG response, as in Table 2, which indicates the current resistance provided by the real structure. A reduction in this resistance is seen as a result of the damaged state of the viaduct. However, to obtain the true value of this reduction would require that the FE analysis has used precisely correct input parameters, which could not be confirmed for this structure.

Figure 13(a) shows the impact that varying the soil spring boundary conditions has on the pier-to-pier span opening response of FE Model 1. In calculating the soil springs, the material properties of soil used were as shown in Table 1; these values are based on the description of the soil as a “sandy clay.” Wolf’s equations also require knowledge of the embedment and dimensions of the foundations, which were not known from record drawings and so had to be estimated in the manner described earlier.

Figure 13(b) summarises a check of the remaining boundary conditions, as described earlier. To arrive at this figure, identical boundary conditions were applied to the outer spans of models containing five and seven arch spans respectively, and the responses of the central spans were then compared to FBG data.

DISCUSSION

1) Comparison of Monitoring Data and Modelling Results

Given the existing damage to the viaduct, some nonlinearity is unquestionably present in its real behaviour. Furthermore, variation exists between the various monitored spans due to uneven distribution of damage, so a linear-elastic model will agree better with some measurements. On top of this, uncertainty in some input parameters for the FE simulations means that comparing magnitudes between FE output and monitoring data is not always informative. However, varying these parameters will only affect the magnitude of the linear-elastic results, not their pattern. It is by searching for similarity, or the lack thereof, in the pattern of the response that interesting conclusions can be drawn. Where there is significant difference, this indicates that damage has led to a different mode of response. This can

potentially be useful in estimating the regions of critical damage, since these should be the regions in which there is a largest deviation from the linear-elastic mode of response.

First inspection of Figure 10 would suggest that the monitored pier-to-pier response at Marsh Lane viaduct can be well reproduced in pattern by a linear-elastic model which includes sufficient structural detail. Furthermore, both Models 3 and 4 produce responses that are very similar in magnitude to the FBG measurements, while Models 1 and 2 are much less stiff, and as a result significantly over-predict this response. This is important because the linear-elastic models are intended to simulate the viaduct before the advent of any significant damage, which would result in a loss of stiffness. Therefore, models which suggest a notably larger magnitude of response than is seen in the FBG data cannot be physically correct.

Since the highest reasonable estimated values of input parameters have been used throughout all FE models, it appears that Models 1 and 2 do not include sufficient structural information and that only by including the effects of both spandrel walls and rigid backing can the true scale of the response be emulated. Even if the soil springs have been underestimated, the “fully fixed” response of Figure 13(a) would not give the necessary decrease in magnitude that is required for Model 1 to produce physically sensible results.

The key remaining uncertainties in the FE models are the masonry Young’s modulus and the horizontal and rotational soil springs K_h and K_r , which could not be calibrated on site. The FE models have all used a value of 5 GPa for the masonry Young’s modulus. In general, historic masonry can have a Young’s modulus in the range 1 – 10 GPa, though it is unlikely for 5 GPa to be exceeded (Augenti, Acconcia & Parisi, 2012). However, the low value of 1 GPa would imply

extensive damage. The Italian seismic design code recommends a value of 3.6 GPa for historic masonry which may be damaged; this is a more likely lower bound (EUCENTRE, 1987). After factoring in the additional constraint that FE Model 4 must produce a response that is no larger in magnitude than that observed in the monitoring data, the required lower bound increases to roughly 4.6 GPa, which is very close to the 5 GPa that has been used.

Similarly, the estimated values of the soil springs correspond to lower bounds of their likely values. However, in this case the vertical soil spring K_v was found to increase substantially upon calibration, and it is not unreasonable to assume that the remaining springs K_h and K_r have been similarly under-estimated. Since the recalibrated vertical spring is comparable to fully fixing the pier bases in vertical translation, this suggests that the true soil conditions could approach the limiting case of fully fixed pier bases.

In Figure 10 onwards, interpolation between the discrete results from FE analysis is achieved using a shape-preserving piecewise cubic interpolation. This approach was found to best preserve smoothness in the simulated response, while minimising any unphysical oscillation. This allowed for simpler visual comparison of the modelling output and the measured patterns of response, although all numerical comparisons only make use of the point measurements obtained directly from the FE models. However, interpolation has not been carried out for the barrel in-plane strains in Figure 12; the patterns of response seen in the FBGs here have changed significantly and there are now different salient points, so that interpolation between the FE results would no longer be meaningful.

In Figure 11, the variation between the monitored response at the four locations, L1 to L4, immediately highlights the uneven distribution of damage across the viaduct, which means that the response no longer maintains the symmetry that would be anticipated in an ideal structure. In particular, there is a pronounced difference in response between the North (L1 and L3) and South (L2 and L4) sides of the viaduct; the response on the North side is consistently larger in magnitude and this corresponds to its higher damage level, relative to the South side (Ye *et al.*, 2018). Given this, it makes sense that the FE simulations reliably show greater similarity to monitoring data for the South side, as they are a closer representation of the less damaged regions of the viaduct.

Figure 12 then considers the strain distribution over the arch barrel. The clearest disagreement occurs when strain is measured across a transverse crack; this is the case for FBG line L1 at point S2 and for L3 at point S7. Line L2 also crosses a transverse crack at point S8, though this is less severe. Other than this, FE results show a reasonable proximity to monitoring data, particularly over the central region of the arch and for lines L2 and L4, which show the response of the less-damaged, Southern half of the viaduct.

In general, there is less clear similarity in response pattern between the FE simulations and monitoring data than there was for the parameters examined in Figure 11. This is compounded by the fact that analysis steps 1 to 9, which were chosen based on the pier-to-pier span opening response, no longer necessarily represent salient points for the strain distribution at all point of the arch. The best similarity in pattern is obtained over the central region of the arch, particularly at points S4 and S5 where the response is close to the characteristic traces seen in

Figure 11. However, at points closer to the arch haunches the response no longer seems to exhibit this form.

Having said this, there is less disagreement when only the response over the Southern half of the viaduct is considered. Examining points S1 and S8, peak strains of -10 to $-20 \mu\epsilon$ are well-matched, though the relaxation when load is removed is not predicted and a transverse crack colours the results for line L2 at point S8. It is possible that relaxation under the removal of load would be better predicted by a model which accounted for the possibility of a cracked interface between the arch haunches and rigid backing, but this was not possible while working within linear-elastic limitations. Likewise, at points S2 and S7, simulated peak strains of -20 to $-30 \mu\epsilon$ show reasonable consistency with the least-damaged line, which is L2 for point S2 and L4 for point S7.

For brevity, Figure 12 only presents strains from Model 4. The strain distributions from Models 1 to 3 were found, through least squares error minimisation, to have worse agreement in pattern relative to the FBG data. This suggests that Model 4 is the linear-elastic simulation that most closely resembles the true distribution of deformation throughout the arch barrel, although that does not mean that Model 4 is correct. What can be said, however, is that this indicates that the true response mode involves some degree of interaction between the arch barrel and both the spandrel walls and rigid backing material. When these interaction effects are not modelled, the corresponding simulated strain pattern deviates further from the true response. Even though it is incorrect for Model 4 to assume full connectivity of these structural components, this has a smaller impact than not modelling them at all.

Furthermore, in order for the strain results from Models 1 to 3 to approach the monitoring data in magnitude, unrealistically high values of masonry Young's Modulus would have to be used in the FE analysis. It is therefore concluded that Model 4 represents the best linear-elastic approximation of the real mode of deformation.

Despite the sensitivity of the local strain distribution to damage, which can affect its response pattern, it is noteworthy that the parameters considered in Figure 11 show roughly the same pattern even when there is significant difference in the extent of damage between the two halves of the viaduct. However, since the measurement locations of these parameters are not close to the damaged regions of these arches, it is perhaps not surprising that the damage has had little impact on the patterns of these measurements. There is little cracking near to the arch crown, where vertical displacement and in-plane strain have been monitored, and although there has been significant deterioration of the arch haunches, this is not picked up in the pier-to-pier measurements because these are taken between the skewbacks.

Although these are common measurements for asset engineers to prescribe, seen as characteristics that can give an impression of the "global" response of the overall arch, it follows that they may not be the most effective. Interpretation of the magnitudes of these measurements is only meaningful if it can be carried out against a benchmark, which could either be measurements prior to damage or an FE model with fully accurate input parameters. Since it is frequently impractical to ascertain these parameters, which have been shown in this study to significantly affect the output of FE simulations, measurement of "global" arch characteristics such as these will often remain opaque until their repetition allows for the tracking of changes.

However, if the monitoring location were to be revised to a point where damage is more commonly seen in masonry arch bridges, then the pattern of the measured response, as well as the magnitude, could offer some useful information about the severity of any nonlinearities. Since damage is often seen on the arch intrados close to the vertical level of rigid backing, due to the sudden step change in stiffness at this level, potential contenders for future “single point” monitoring could well be the third or quarter point of the span, as opposed to the arch crown. In particular, strain measurements at these locations are likely to be illuminating and warrant investigation in future work.

2) Contributions of Structural Components to Overall Behaviour

The contributions to global resistance, against deformation under serviceability loads, are shown in Table 2 for the various structural components. Often, simplifying assumptions will be made during analysis of masonry arch bridges and viaducts. For example, an “effective width” model may neglect the positive effects of the spandrel walls. Table 2 shows the size of the contribution that would be neglected in this case, if such a calculation were to be performed under serviceability conditions. Likewise, the presence of rigid backing material above the arch haunches provides a further stabilising effect which increases the global resistance of the structure to deformation.

The values of Table 2 are in rough agreement with other results in the literature, which give corresponding ULS predictions of contributions from these components (Boothby, Domalik & Dalal, 1998; Fanning, Boothby & Roberts, 2001; Brencich, Cassini & Pera, 2016). One point in particular is worth noting: the contribution of spandrel walls is higher under service conditions than it seems to be at ULS. When a multi-span masonry arch bridge is at its ultimate capacity,

Fanning *et al.* suggest that a contribution towards this capacity of 30% comes from the spandrel walls. The results of this study suggest that the contribution of spandrel walls is 48% in serviceability conditions, a significant increase. In all likelihood, this is because partial spandrel wall separation can be expected to occur before the ultimate capacity is reached, so that by this point the effectiveness of the spandrel walls will have been reduced.

Another interesting observation is that the inclusion of relieving arches in Model 4 does not lead to a more flexible response, despite the reduction in pier stiffness that this results in. Instead, it can be concluded that the response is more sensitive to the stiffness of the spandrel walls and rigid backing. A marginal reduction in pier stiffness has a negligible impact, because these already offer little resistance against flexural deformation.

Figure 13(a) summarises the work that was done to investigate parameter variation in the uncertain soil springs. For very soft springs in all degrees of freedom, the pattern of span opening is no longer properly replicated. There is, therefore, a minimum amount of restraint which must be applied to the pier bases before the modelled behaviour will capture the true span-to-span response of the real viaduct. Additionally, springs of this softness are unlikely to be realistic, since these would be far softer than the stiffnesses suggested by Wolf's equations.

The response under the applied soil springs is very similar to that which is obtained by releasing the pier bases in rotation and horizontal translation. In other words, the recalibrated vertical soil springs, in combination with horizontal and rotational springs calculated using Wolf's equations, produce a very similar outcome to simply fixing the pier bases in vertical translation alone. This is perhaps not surprising, given that the recalibrated vertical springs are

considerably stiffer than their horizontal and rotational counterparts. The most likely implication is that the qualitative ground investigations have underestimated the soil conditions, or that the assumed embedment has been underpredicted. However, in the absence of more definite information, it was decided to continue using the current estimates, since these at least constitute a safe lower bound on the true conditions.

It can also be concluded that the overall response is reasonably insensitive to pier rotational springs, since releasing the pier bases in rotation causes only a small change compared to pier bases that are fully fixed. This also indicates that the pier-to-pier span opening is insensitive to the precise mode of response of the piers, which must behave in double curvature bending when their bases are fully fixed, but which will freely rotate as rigid bodies once this degree of freedom is released. This is most likely a consequence of the pier height, which is very large compared to the movements imposed on the piers by span opening and closing.

However, even if the true soil stiffnesses approached the “fully fixed” upper bound, this could at most increase the global resistance to pier-to-pier span opening by fourfold. Meanwhile, Model 1 has seven times less global resistance to this response than is observed in the FBG data. As a result, despite the spandrel separation cracks which are present on the Marsh Lane viaduct, which may well also extend across the arch-backing interface, it is impossible to achieve the observed structural resistance to deformation without including some effect from either or both of the rigid backing and the spandrel walls.

Figure 13(b) examines the impact of the boundary conditions which have been enforced on the outer spans of the FE simulations. These boundary conditions themselves are artificial but have been implemented to account for the continuity of the viaduct beyond the modelled spans. Results are only extracted for the central span of the model, so it is necessary that this span is sufficiently removed from the outer boundary conditions. In the figure, a comparison is made between models containing five and seven spans. The responses show negligible difference, and so it can be concluded that, in both models, these boundary conditions are sufficiently remote from the central span that they do not influence the results in this region of interest. Although Figure 13(b) considers FE Model 4, similar results were achieved when earlier Models were investigated in the same way. As a result, it was decided to consider only five spans in the FE models, as this reduced computation time.

Further Comments on the FE Simulations

Based on these findings, FE Model 4 appears to offer the closest approximation of real behaviour that can be achieved using a linear-elastic model. However, it also assumes full connectivity of the various structural components, which may not be realistic and warrants further discussion.

The assumption of full connectivity can be investigated by examining stresses at the arch-spandrel interface. At the lower edges of the spandrel walls, these are in the range +0.25 MPa to -1 MPa; negligible tensile strength means that this is sufficient to cause separation cracks between the arch and spandrels. Such cracks are observed at the viaduct. It is not possible to investigate any radial tensile stresses within the arch at the arch-backing interface, because the

backing has not been explicitly modelled and the arch is composed of shell elements, with the corresponding assumptions that stresses in the radial, i.e. out-of-plane, direction are zero.

Although there is no visible evidence of inter-ring shear failure at the Marsh lane viaduct, and the presence of inter-locking header bonds should increase shear resistance and mitigate the possibility of inter-ring shear cracking, this can be further investigated in the output of FE Model 4. In this model, there is not much variation of shear stress over the depth of the arch, which is 4 brick rings in thickness. For the majority of the arch, extreme shear stresses are in the range ± 0.2 MPa, with linear variation of shear stress over the depth of the arch. However, close to the spandrel walls this range increases to ± 0.3 MPa.

The Italian code for historic masonry suggests a maximum value of shear resistance of 0.18 MPa for full brickwork with lime mortar (EUCENTRE, 1987). It therefore follows that typical values of extreme shear stress are at the limit which can be resisted by historic masonry brickwork, and exceed this limit close to the spandrel walls so that separation of the arches from the spandrels might be expected. However, at the inter-ring interfaces over the arch depth, shear stresses are consistently below this limit. This aligns with the visible evidence on site, where there is cracking between the arch and the spandrel, but not between the individual arch rings.

From this, it can be concluded that FE Model 4 exhibits some non-physical behaviour. The inability to transmit tensile stresses between the arch and spandrels means that its estimations of deflections under load are lower bounds on the true response. Real behaviour is likely to lie between the limiting cases of Models 1 and 4. Within the limits of linear-elastic methods, the

similarity in response pattern for Model 4, at least for parts of the arch with low damage, suggests that it offers a better simulation than other, more simplified models.

CONCLUSIONS

In this study, linear-elastic finite element models were compared with the actual service response of a masonry arch railway viaduct, under its operational loads, which was evaluated using monitoring technologies.

Because of parameter uncertainty, it was necessary to make reasonable assumptions about the material properties, non-visible geometry and boundary conditions. With these in place, it was found that the output of FE simulations was similar in pattern to typical monitoring data for common “global” arch measurements, such as the vertical crown displacement and pier-to-pier span opening displacement. Although there was also similarity in magnitude for the more detailed models, uncertainty remains with regard to the input parameters and, as such, conclusive interpretation of the response magnitude is not possible.

“Local” measurements of the distribution of barrel in-plane strains offered less similarity in pattern between modelling and monitoring results; however, this is to be expected given the damaged condition of the viaduct and indeed suggests that there may be potential to exploit these “local” measurements in the future for more insightful monitoring of these structures. In this context, linear-elastic analysis provided a useful simplification of the “pre-damage” behaviour, against which “local” measurements could be evaluated to gauge the severity and the extent of impact of any damage, in cases where more thorough modelling is impractical.

However, it is important to emphasise that the magnitude of these FE simulations is very difficult to verify; this is the case for more complex analyses as well as linear-elastic methods.

For the Marsh Lane viaduct in particular, it was found that the transverse cracking damage caused a local change in strain response patterns, and to a lesser degree global changes, such as increase in vertical crown displacements. Regions of low visible damage display a pattern of response that is similar to the linear-elastic idealisation, which suggests that they do indeed remain healthy.

Furthermore, this study has quantified the relative contributions to global serviceability behaviour that come from the various structural components making up a masonry arch viaduct. The results demonstrate that while neglecting major structural components may be a useful and conservative assumption for ULS assessment, these components must be considered when evaluating SLS behaviour.

ACKNOWLEDGEMENTS

This work forms part of a PhD, which is funded through an EPSRC Doctoral Training Partnership (grant reference number EP/M506485/1). Data collection was made possible by the Cambridge Centre for Smart Infrastructure and Construction, through additional EPSRC funding (grant reference number EP/L010917/1). The authors would like to thank Melanie Banes and Giuseppe Narciso for their help in the early stages of this project. Additionally, they are grateful to Network Rail for providing access to the Marsh Lane viaduct and for their continued interest in this research.

REFERENCES

- Acikgoz, S., DeJong, M.J., Kechavarzi, C. & Soga, K. (2018a) Dynamic response of a damaged masonry rail viaduct: Measurement and interpretation. *Engineering Structures*. 168, 544–558.
- Acikgoz, S., DeJong, M.J. & Soga, K. (2018b) Sensing dynamic displacements in masonry rail bridges using 2D digital image correlation. *Structural Control and Health Monitoring*. 25 (8).
- Armstrong, D.M., Sibbald, A. & Forde, M.C. (1995) Integrity assessment of masonry arch bridges using the dynamic stiffness technique. *NDT & E International*. [Online] 28 (6), 367–375. Available from: <http://www.sciencedirect.com/science/article/pii/096386959500047X>.
- Augenti, N., Acconcia, E. & Parisi, F. (2012) *MADA: MAsonry DAtabase*. [Online]. 2012. Available from: http://www.reluis.it/index.php?option=com_mada&Itemid=160 [Accessed: 1 August 2017].
- Augustus-Nelson, L., Swift, G., Smith, C., Gilbert, M., et al. (2016) Behaviour of Backfilled Masonry Arch Bridges Subjected To Cyclic Loading. In: *Proceedings of ARCH'16 International Conference on Arch Bridges*. 2016 pp. 1039–1048.
- Boothby, T.E., Domalik, D.E. & Dalal, V.A. (1998) Service Load Response Of Masonry Arch Bridges. *Journal of Structural Engineering (ASCE)*. 124 (January), 17–23.
- Brencich, A., Cassini, G. & Pera, D. (2016) Load Bearing Structure Of Masonry Bridges. In: *Proceedings of ARCH'16 International Conference on Arch Bridges*. 2016 pp. 767–774.

Brencich, A. & Morbiducci, R. (2007) Masonry Arches: Historical Rules and Modern Mechanics. *International Journal of Architectural Heritage*. [Online] 1 (2), 165–189. Available from: doi:10.1080/15583050701312926.

Costa, C., Arêde, A., Morais, M. & Aníbal, A. (2015) Detailed FE and DE modelling of stone masonry arch bridges for the assessment of load-carrying capacity. *Procedia Engineering*. [Online] 114, 854–861. Available from: doi:10.1016/j.proeng.2015.08.039.

DeJong, M.J. & Vibert, C. (2012) Seismic response of stone masonry spires: Computational and experimental modeling. *Engineering Structures*. [Online] 40, 566–574. Available from: doi:10.1016/j.engstruct.2012.03.001.

Domede, N., Sellier, A. & Stablon, T. (2013) Structural analysis of a multi-span railway masonry bridge combining in situ observations, laboratory tests and damage modelling. *Engineering Structures*. [Online] 56, 837–849. Available from: doi:10.1016/j.engstruct.2013.05.052.

EUCENTRE (1987) Italian Seismic Design Code (OPCM 3274/03 and further modifications): structural masonry chapters. In: *Italian Seismic Design Code (OPCM 3274/03 and further modifications)*.

Fanning, P.J. & Boothby, T.E. (2001) Three-dimensional modelling and full-scale testing of stone arch bridges. *Computers and Structures*. [Online] 79 (29–30), 2645–2662. Available from: doi:10.1016/S0045-7949(01)00109-2.

Fanning, P.J., Boothby, T.E. & Roberts, B.J. (2001) Longitudinal and transverse effects in masonry arch assessment. *Construction and Building Materials*. [Online] 15 (1), 51–60.

Available from: doi:10.1016/S0950-0618(00)00069-6.

Forgács, T., Sarhosis, V. & Bagi, K. (2017) Minimum thickness of semi-circular skewed masonry arches. *Engineering Structures*. [Online] 140, 317–336. Available from: doi:10.1016/j.engstruct.2017.02.036.

Gibbons, N. (2014) *Modelling and assessment of masonry arch bridges*.

Gilbert, M. (2017) *LimitState:RING - Masonry Arch Bridge Analysis Software | LimitState*. [Online]. 2017. Available from: <http://www.limitstate.com/ring> [Accessed: 26 August 2017].

Harvey, B. (2017) *Archie-M Homepage*. [Online]. 2017. Available from: <http://www.obvis.com/> [Accessed: 26 August 2017].

Lemos, J. V. (2007) Discrete element modeling of masonry structures. *International Journal of Architectural Heritage*. [Online] 1 (2), 190–213. Available from: doi:10.1080/15583050601176868.

McInerney, J. & DeJong, M.J. (2015) Discrete Element Modeling of Groin Vault Displacement Capacity. *International Journal of Architectural Heritage*. [Online] 9 (8), 1037–1049. Available from: doi:10.1080/15583058.2014.923953.

Network Rail (2013) *Bridge Detailed Examination Report for Marsh Lane Viaduct (HUL4/48)*.

Network Rail (2006) *NR-GN-CIV-025: The Structural Assessment of Underbridges*.

Wolf, J.P. (1994) *Foundation Vibration Analysis Using Simple Physical Models*. 1st edition. Englewood Cliffs, NJ, PTR Prentice Hall.

Ye, C., Acikgoz, S., Pendrigh, S., Riley, E., et al. (2018) Mapping deformations and inferring movements of masonry arch bridges using point cloud data. *Engineering Structures*. 173, 530–545.

Zhang, Y., Macorini, L. & Izzuddin, B.A. (2017) Numerical investigation of arches in brick-masonry bridges. *Structure and Infrastructure Engineering*. [Online] 2479 (July), 1–19. Available from: doi:10.1080/15732479.2017.1324883.

FIGURE CAPTIONS

Fig. 1. Map view showing location of Marsh Lane viaduct arches 37 and 38

Fig. 2. View of the Marsh Lane viaduct

Fig. 3. (a) Main span elevation of Marsh Lane viaduct, and (b) typical pier geometry as viewed along the global longitudinal direction (with key dimensions in metres)

Fig. 4. Overview of key damage affecting arches 37 and 38

Fig. 5. Locations of FBGs, labelled S1 to S8, along the four longitudinal monitoring lines L1 to L4

Fig. 6. Typical span-to-span opening as measured by FBG sensors at Marsh Lane viaduct, for the cases when (top) trains are passing on the track directly above the FBG sensors and when (bottom) trains are passing on the opposite track

Fig. 7. Views of the four FE Models: (a) Model 1, (b) Model 2, (c) Model 3, and (d) Model 4

Fig. 8. The nine analysis steps used in the FE calculations, plotted on a smoothed pier-to-pier response, with corresponding axle locations given below (with dimensions in millimetres)

Fig. 9. Boundary conditions and soil springs, as applied to (a) interior piers and (b) outer piers in the FE models

Fig. 10. Comparison of pier-to-pier span opening between typical FBG data and FE analysis models

Fig. 11. Comparison between FE model 4 and monitoring data for crown vertical displacement, crown in-plane strain, and pier-to-pier span opening

Fig. 12. Comparison of in-plane barrel strain distributions between FE Model 4 and FBG data; symmetric locations from the two halves of the arch are shown side by side

Fig. 13. (a) The impact of varying soil spring stiffnesses on the pier-to-pier opening response of FE Model 1, and (b) the difference in pier-to-pier opening responses for versions of FE Model 4 containing five and seven spans

TABLES

Table 1. Assumed values of input parameters for FE simulations

Parameter:	Assumed Value:
Young's Modulus of masonry, $E_{masonry}$	5 GPa
Poisson's ratio of masonry, $\nu_{masonry}$	0.2
Density of masonry, $\rho_{masonry}$	1600 kg/m ³
Young's Modulus of soil, E_{soil}	250 kPa
Poisson's ratio of soil, ν_{soil}	0.3
Soil vertical spring K_v	984x10 ⁶ N/m
Soil horizontal spring K_h	2.30x10 ⁶ N/m
Soil rotational spring K_r	12.5x10 ⁶ Nm

Table 2. Resistance against pier-to-pier span opening deflections, as provided by the various FE models and the real viaduct

Model	Model 1	Model 2	Model 3	Model 4	Real Viaduct
Structural elements added in this model	Piers, arches, and soil springs (basic model)	Spandrel walls	Rigid backing above arch haunches	Relieving arches (final model)	---
Contribution to global resistance from additional element(s)	13%	48%	39%	0%	---
Cumulative global resistance to deformation	13%	61%	100%	100%	91%

FIGURES

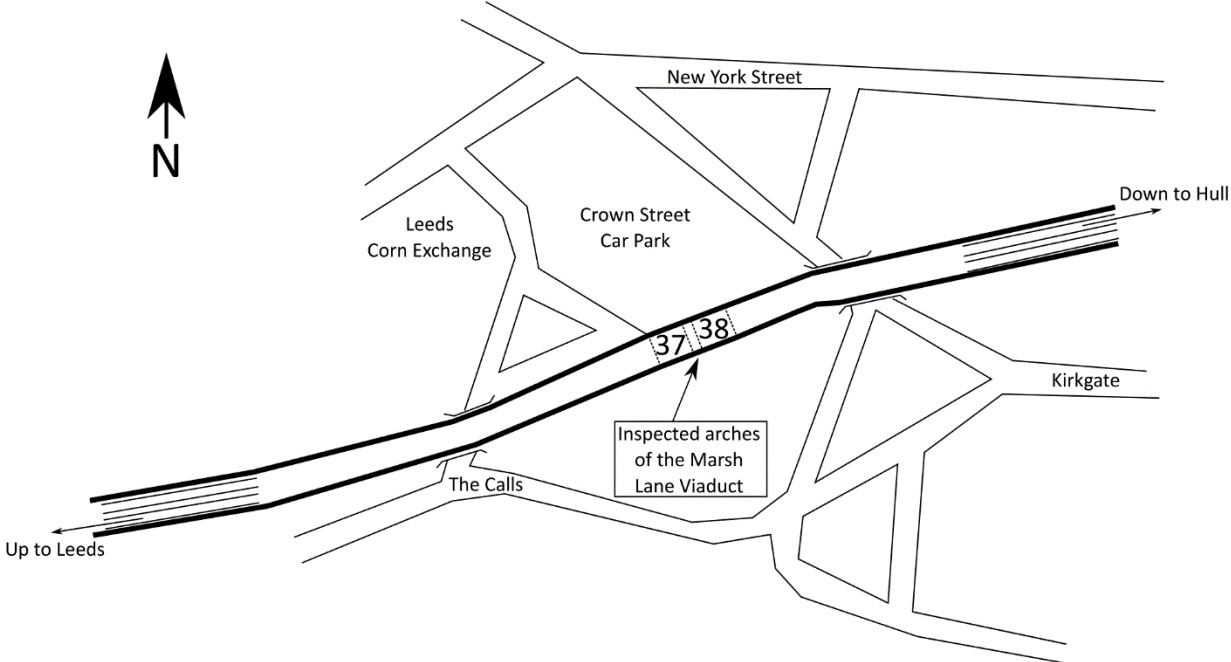


Fig. 1. Map view showing location of Marsh Lane viaduct arches 37 and 38



Fig. 2. View of the Marsh Lane viaduct

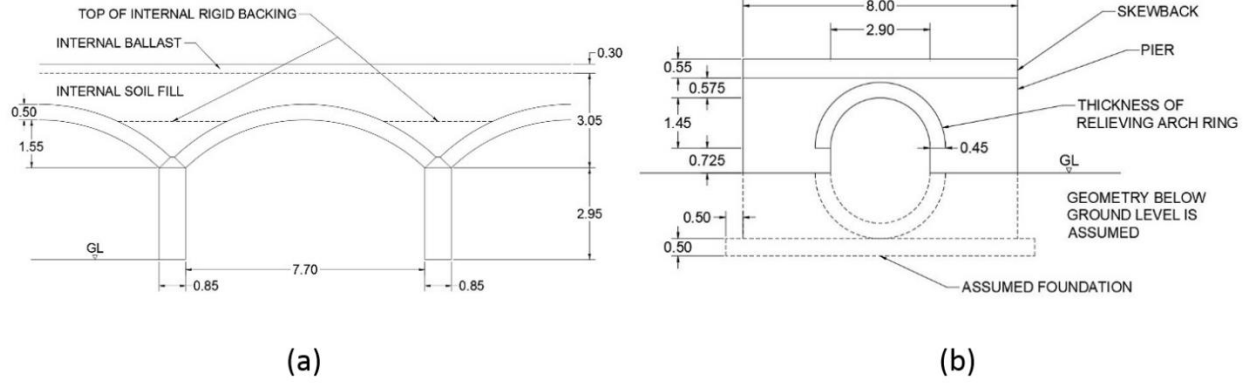


Fig. 3. (a) Main span elevation of Marsh Lane viaduct, and (b) typical pier geometry as viewed along the global longitudinal direction (with key dimensions in metres)

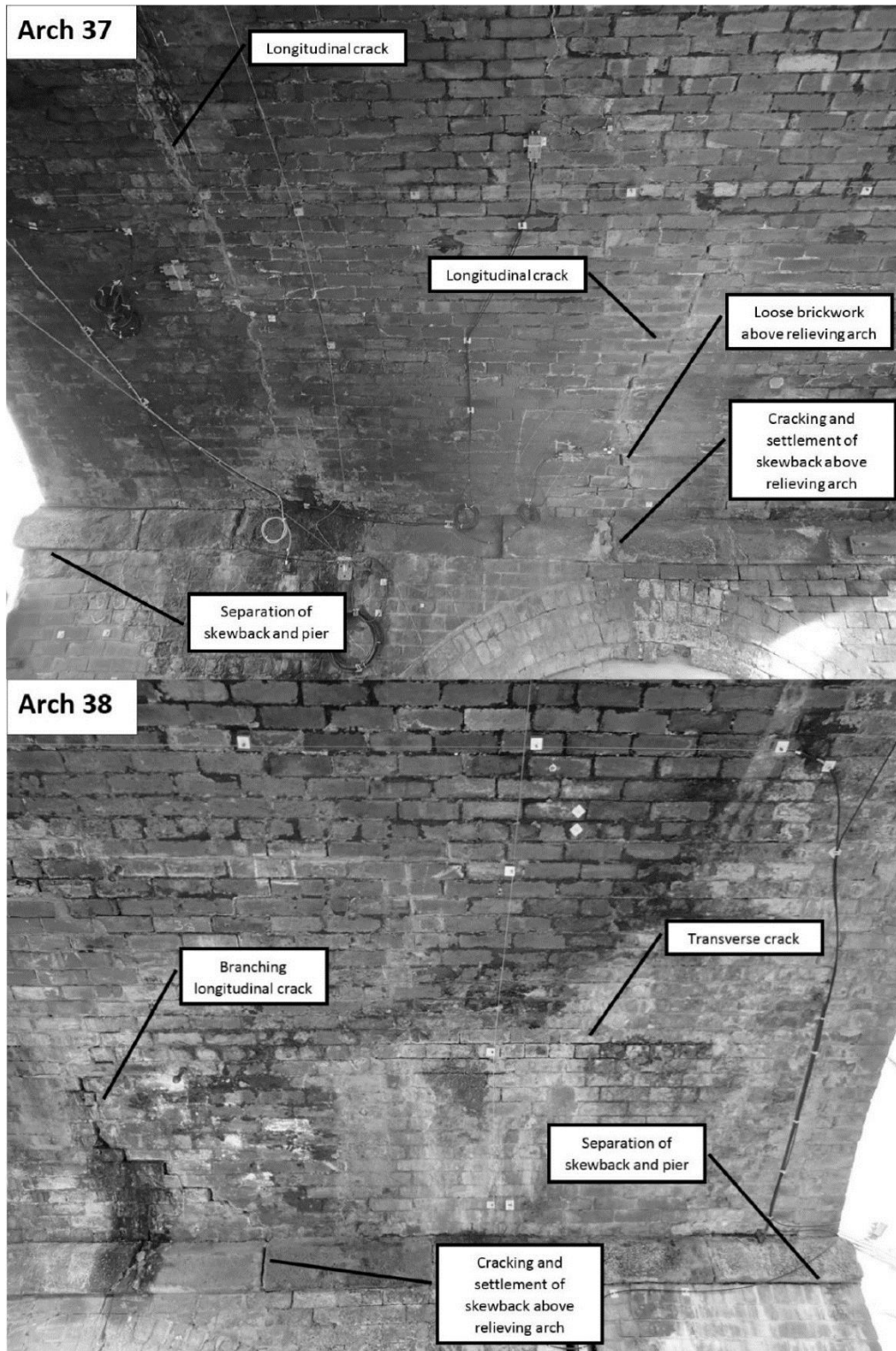


Fig. 4. Overview of key damage affecting arches 37 and 38

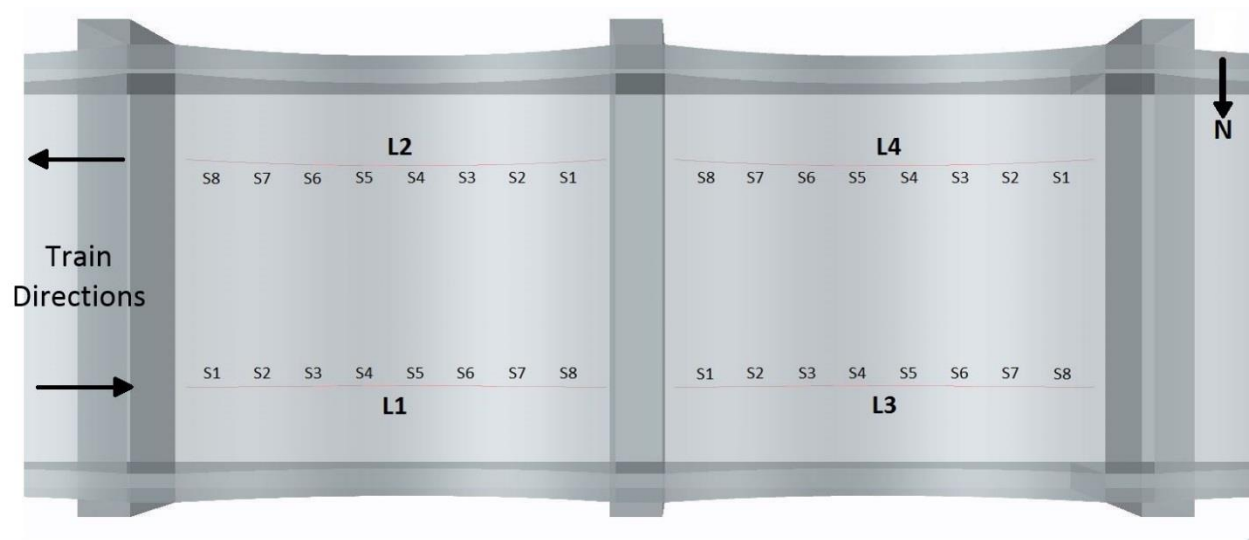


Fig. 5. Locations of FBGs, labelled S1 to S8, along the four longitudinal monitoring lines L1 to L4

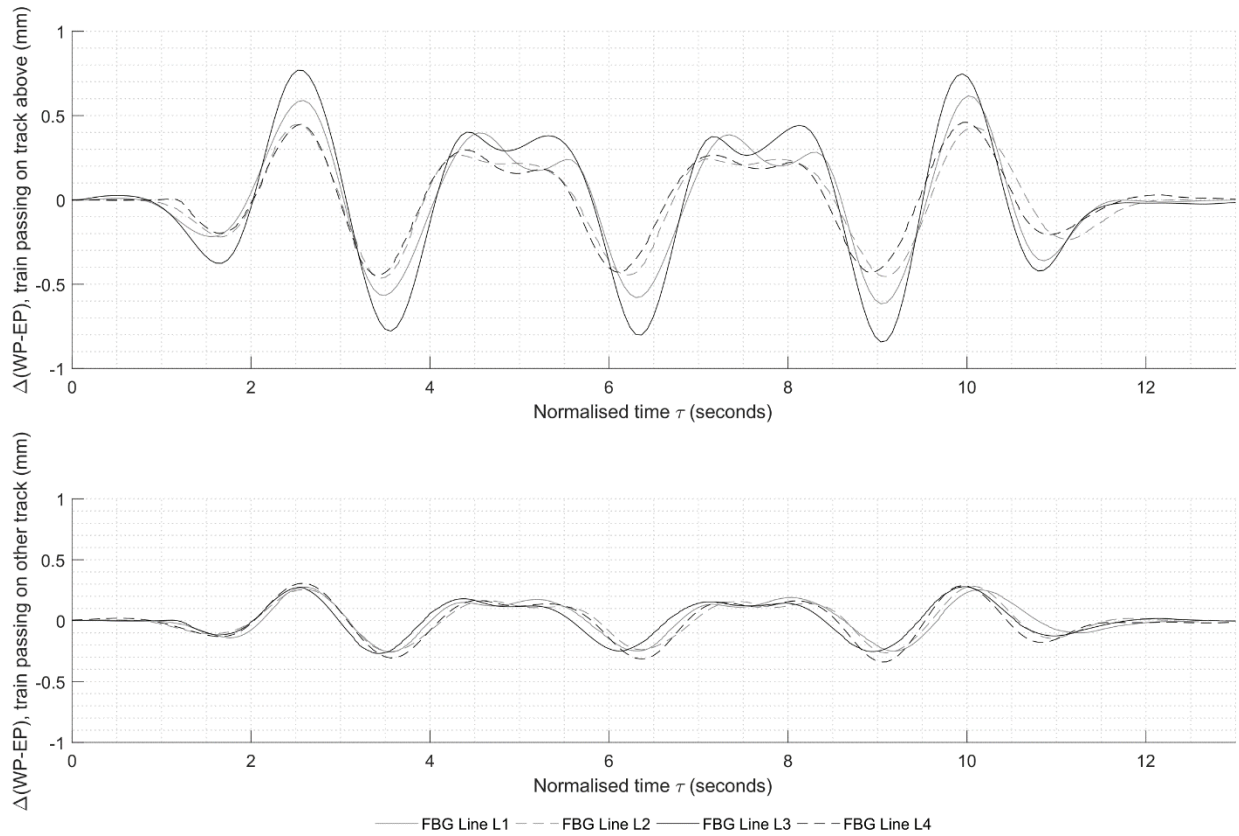


Fig. 6. Typical span-to-span opening as measured by FBG sensors at Marsh Lane viaduct, for the cases when (top) trains are passing on the track directly above the FBG sensors and when (bottom) trains are passing on the opposite track

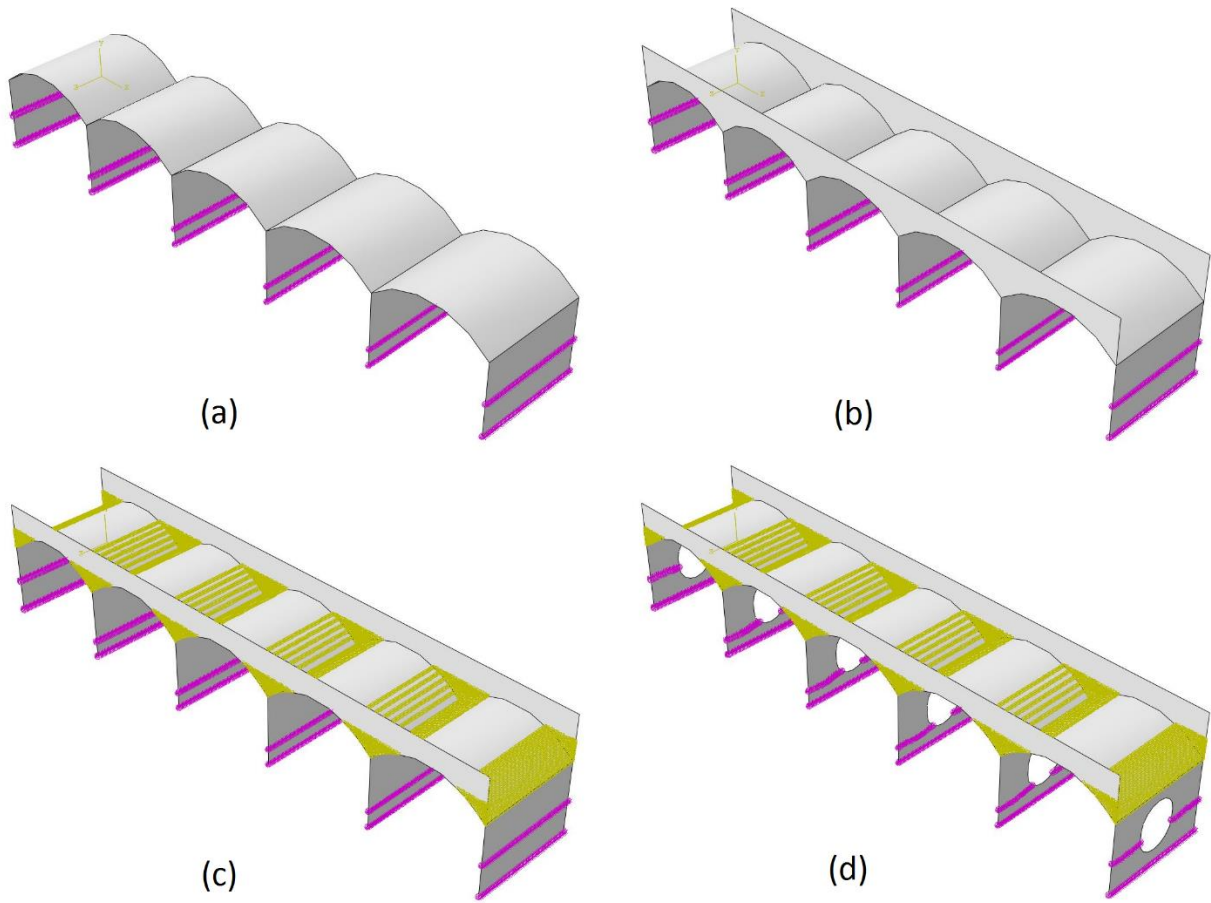


Fig. 7. Views of the four FE Models: (a) Model 1, (b) Model 2, (c) Model 3, and (d) Model 4

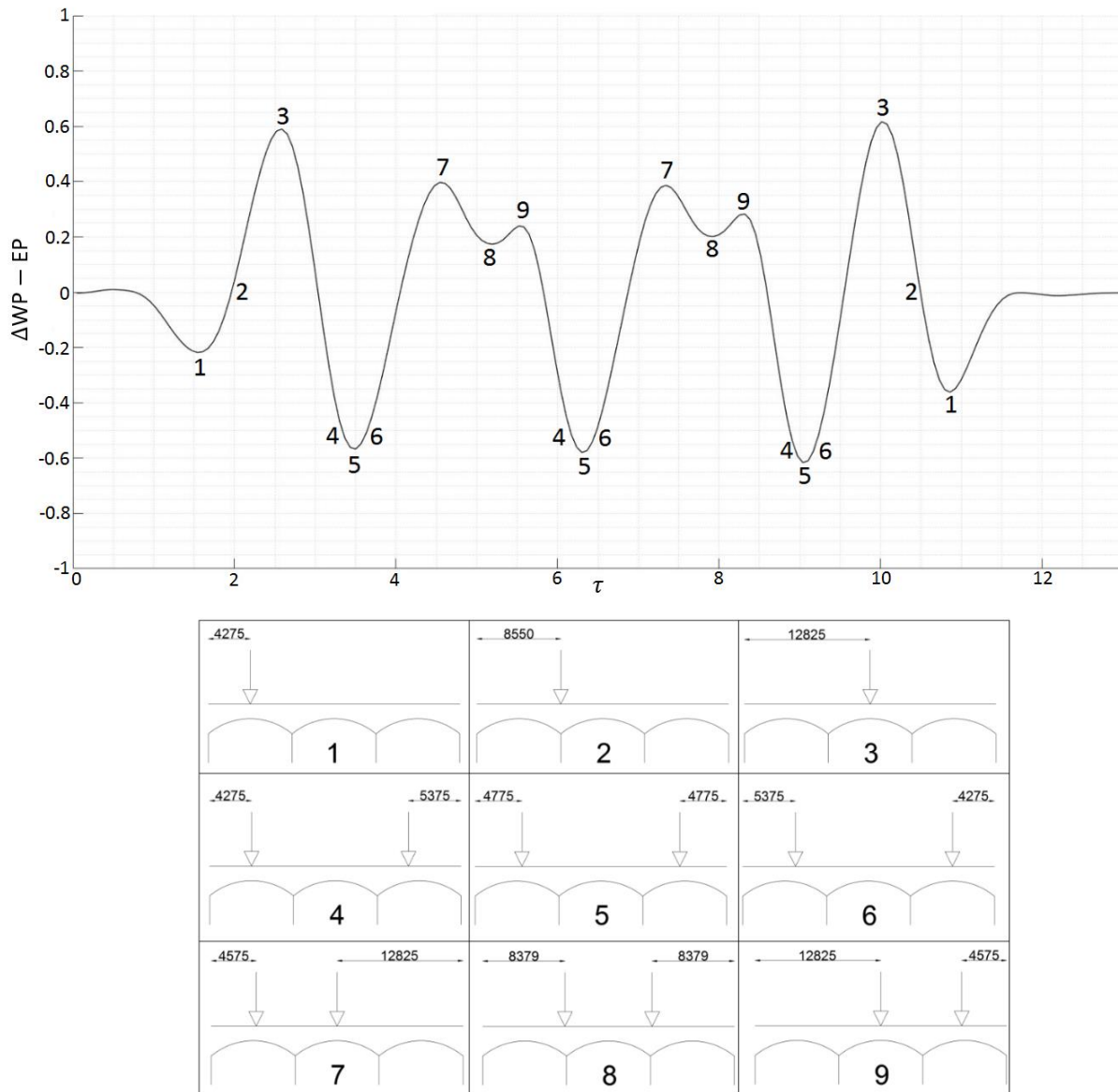


Fig. 8. The nine analysis steps used in the FE calculations, plotted on a smoothed pier-to-pier response, with corresponding axle locations given below (with dimensions in millimetres)

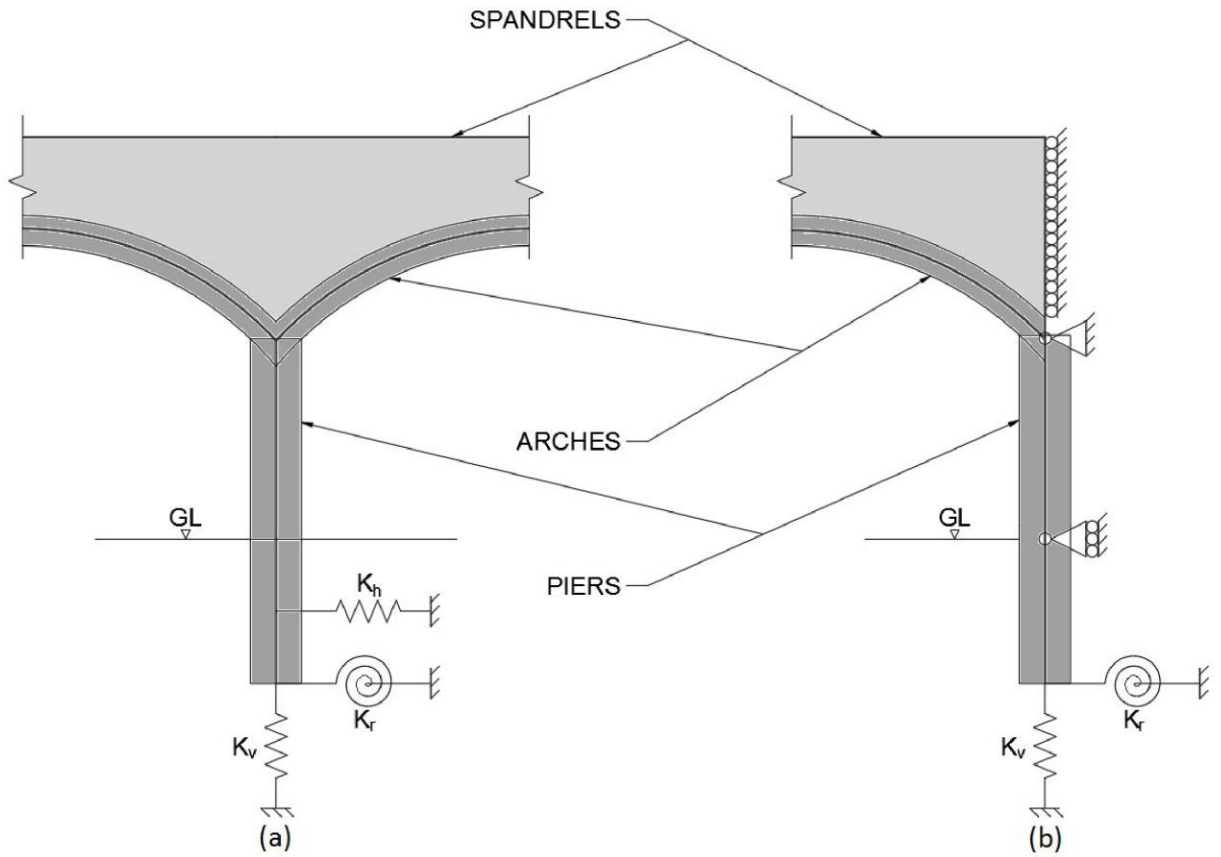


Fig. 9. Boundary conditions and soil springs, as applied to (a) interior piers and (b) outer piers in the FE models

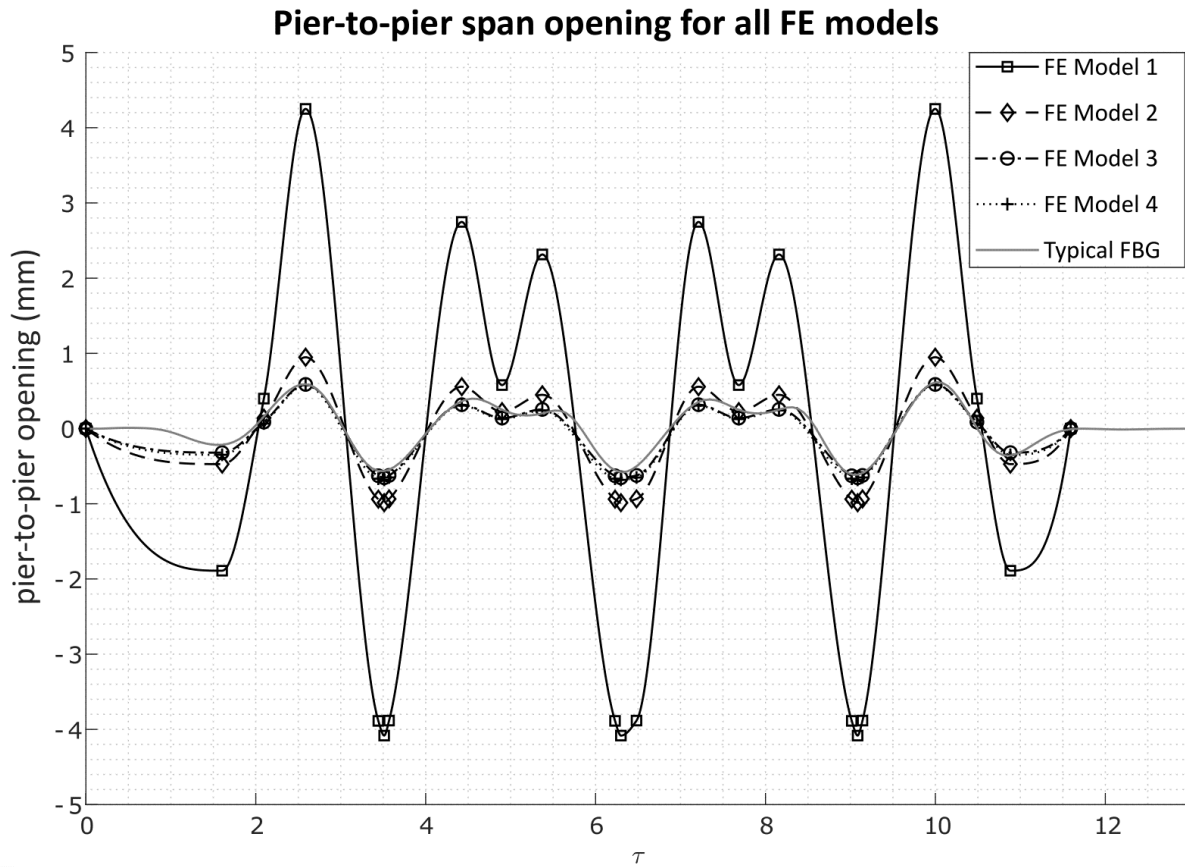


Fig. 10. Comparison of pier-to-pier span opening between typical FBG data and FE analysis models

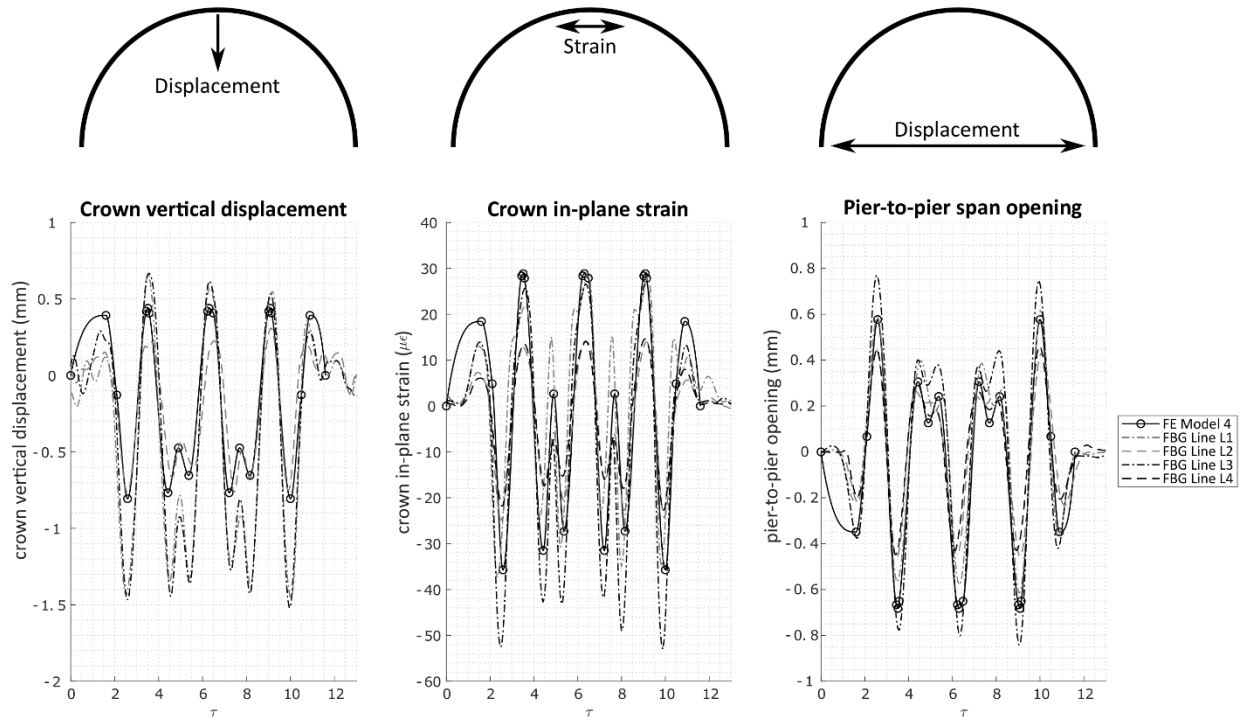


Fig. 11. Comparison between FE model 4 and monitoring data for crown vertical displacement, crown in-plane strain, and pier-to-pier span opening

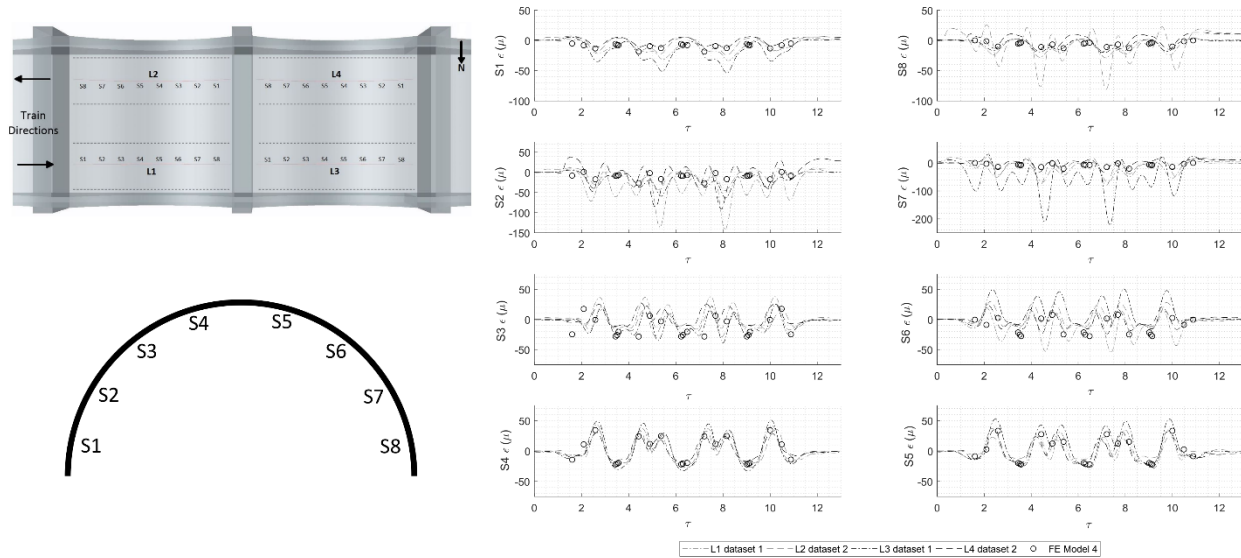
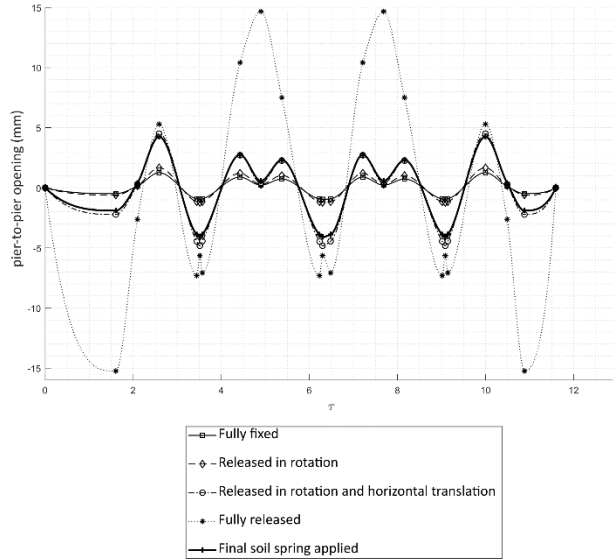
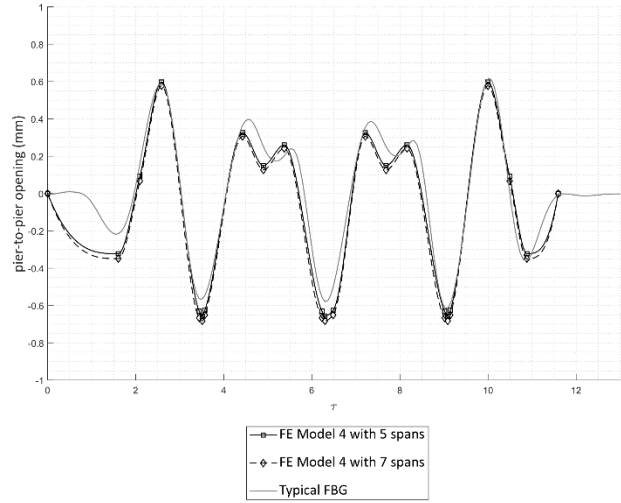


Fig. 12. Comparison of in-plane barrel strain distributions between FE Model 4 and FBG data; symmetric locations from the two halves of the arch are shown side by side



(a)



(b)

Fig. 13. (a) The impact of varying soil spring stiffnesses on the pier-to-pier opening response of FE Model 1, and (b) the difference in pier-to-pier opening responses for versions of FE Model 4 containing five and seven spans